

JGR Biogeosciences

RESEARCH ARTICLE

10.1029/2020JG006116

Key Points:

- Net primary production (NPP) derived from Argo-based bio-optical measurements was comparable and complementary to ^{14}C incubation and satellite estimates
- Both Carbon-based Productivity Model and Photoacclimation Productivity Model have their own advantages and limitations
- NPP profiles showed varying seasonal NPP distribution patterns along a North-South transect in the western North Atlantic Ocean

Supporting Information:

- Supporting Information S1

Correspondence to:

B. Yang,
boyang@mail.usf.edu

Citation:

Yang, B., Fox, J., Behrenfeld, M. J., Boss, E. S., Haëntjens, N., Halsey, K. H., et al. (2021). In situ estimates of net primary production in the western North Atlantic with Argo profiling floats. *Journal of Geophysical Research: Biogeosciences*, 126, e2020JG006116. <https://doi.org/10.1029/2020JG006116>

Received 13 OCT 2020

Accepted 15 DEC 2020

In Situ Estimates of Net Primary Production in the Western North Atlantic With Argo Profiling Floats

Bo Yang^{1,2,3} , James Fox⁴, Michael J. Behrenfeld⁵ , Emmanuel S. Boss⁶, Nils Haëntjens⁶ , Kimberly H. Halsey⁴ , Steven R. Emerson⁷ , and Scott C. Doney¹ 

¹Department of Environmental Sciences, University of Virginia, Charlottesville, VA, USA, ²Rosenstiel School of Marine and Atmospheric Science, Cooperative Institute for Marine and Atmospheric Studies, University of Miami, Miami, FL, USA, ³Atlantic Oceanographic and Meteorological Laboratory (AOML), NOAA, Miami, FL, USA, ⁴Department of Microbiology, Oregon State University, Corvallis, OR, USA, ⁵Department of Botany and Plant Pathology, Oregon State University, Corvallis, OR, USA, ⁶School of Marine Sciences, University of Maine, Orono, ME, USA, ⁷School of Oceanography, University of Washington, Seattle, WA, USA

Abstract The ^{14}C incubation method for net primary production (NPP) has limited spatial/temporal resolution, while satellite approaches cannot provide direct information at depth. With chlorophyll-a and backscatter measurements from BGC-Argo floats, we quantified year-round NPP in the western North Atlantic Ocean using both the Carbon-based Productivity Model (CbPM) and Photoacclimation Productivity Model (PPM). Comparison with NPP profiles from ^{14}C incubation measurements showed advantages and limitations of both models. CbPM reproduced the magnitude of NPP in most cases. However, in the summer the CbPM-based NPP had a large peak in the subsurface, which was an artifact from the subsurface chlorophyll maximum caused by photoacclimation. PPM avoided the artifacts from photoacclimation, but the magnitude of PPM-derived NPP was smaller than the ^{14}C result. Different NPP distribution patterns along a North-South transect in the Western North Atlantic Ocean were observed, including higher winter NPP/lower summer NPP in the south, timing differences in NPP seasonal phenology, and different NPP depth distribution patterns in the summer months. Using a 6-months record of concurrent oxygen and bio-optical measurements from two Argo floats, we also demonstrated the ability of Argo floats to obtain estimates of the net community production to NPP ratio, ranging from 0.3 in July to -1.0 in December 2016. Our results highlight the utility of float bio-optical profiles and indicate that environmental conditions (e.g., light availability, nutrient supply) are major factors controlling the seasonality and spatial (horizontal and vertical) distributions of NPP in the western North Atlantic Ocean.

1. Introduction

Biological productivity by upper-ocean phytoplankton communities is central to marine biogeochemistry, carbon cycling, and ecosystem health. Phytoplankton net primary production (NPP), defined as gross photosynthetic carbon fixation minus the carbon respired by phytoplankton themselves, is a key metric of biological productivity. Traditional methods for NPP measurements rely on ship-based discrete sampling and bottle incubations (e.g., ^{14}C incubation), which introduce potential artifacts and limit the spatial and temporal coverage of the global ocean. Over the past several decades, the establishment of operational ocean-observing satellite networks made it possible to make reasonable estimates of large-scale ocean NPP patterns. The global distribution of NPP has been estimated using satellite observations with the Vertically Generalized Production Model (VGPM, Behrenfeld & Falkowski, 1997) and Carbon-based Productivity Model (CbPM, Behrenfeld et al., 2005; T. Westberry et al., 2008). However, the satellite remote sensing approach cannot provide direct information at depth, and also lacks coverage in regions with high solar zenith angles or obscured by clouds.

The development of instruments/sensors on underway and autonomous platforms provides a complementary approach to ship-based ^{14}C incubation and satellite remote sensing methods. As an example of the application of underway surface measurements, Burt et al. (2018) combined underway bio-optical measurements and mass spectrometry to study spatial distributions of NPP, net community production (NCP), and the NCP to NPP ratio in subarctic Northeast Pacific surface waters during the spring/summer growth season (May to July). As for previous depth-resolved studies using in situ autonomous platforms, the 2008

North Atlantic Bloom Experiment (NAB08) used Lagrangian floats and a Seaglider to obtain high-resolution measurements within a single phytoplankton patch in the subarctic North Atlantic (59°N to 62°N) during the spring bloom from April to May (Alkire et al., 2012). During the NAB08 experiment, phytoplankton biological carbon production was studied in the context of NPP (derived from bio-optical measurements, Briggs et al., 2018), particulate organic carbon (POC, derived from bio-optical measurements, Alkire et al., 2012), and NCP (derived from oxygen and nitrate mass balance, Alkire et al., 2012). A similar experiment with autonomous floats was conducted later in the subtropical North Atlantic near Bermuda Atlantic Time-Series (BATS) stations from 2013 to 2014, in which a modified CbPM model was used for NPP estimation (Estapa et al., 2019).

The western North Atlantic Ocean is an area with one of the most significant, open-ocean phytoplankton seasonal blooms in the global ocean. From 2015 to 2018, a time-series study was conducted in this region during the North Atlantic Aerosols and Marine Ecosystems Study (NAAMES, <https://naames.larc.nasa.gov/>) funded by the National Aeronautics and Space Administration (NASA). The objective of NAAMES was to study the key processes controlling ocean system function, their influences on atmospheric aerosols, and their implications for climate (Behrenfeld et al., 2019). Four research cruises were conducted from 2015 to 2018, with comprehensive shipboard sampling and measurements of biological production (including ^{14}C incubation experiments for NPP). Biogeochemical Argo (BGC-Argo) floats were deployed during these campaigns, thereby providing a unique opportunity for comparisons between shipboard measurements and Argo float measurements. In our previous work, we used the NAAMES BGC-Argo data to analyze the phytoplankton phenology in the context of phytoplankton growth rate and carbon accumulation rate (Yang et al., 2020). In this study, we use the BGC-Argo data to derive depth-resolved NPP with two different bio-optical models. The Argo-based NPP is first evaluated against ^{14}C incubation NPP data from the NAAMES cruises, followed by an analysis of the spatial and temporal distributions of NPP in the western North Atlantic. We also demonstrate the possibility of obtaining in situ seasonal NCP to NPP ratios, using a 6-month concurrent record of bio-optical and oxygen measurements from two Argo floats.

2. Methods

2.1. Research Area

This study utilized field data from the NASA North Atlantic Aerosol and Marine Ecosystem Study (NAAMES, Behrenfeld et al., 2019). Our research area, located in the North Atlantic Ocean between 39°N and 54°N and 36°W to 46°W (Figure 1), was divided into northern (more temperate) and southern (more subtropical) regions with the partition at 47°N, roughly following the categorization by Della Penna and Gaube (2019).

2.2. In Situ Bio-Optical Measurements

Chlorophyll-*a* (*Chl-a*) concentration, phytoplankton carbon biomass (C_{phyto}), salinity (*S*), temperature (*T*), and pressure (*P*) data used for NPP calculation were obtained from five BGC-Argo floats (n0572, n0849, n0850, n0851, n0852, WMO number 5902460, 5903106, 5903107, 5903108, and 5903109) deployed by the University of Maine (Figure 1). These five floats were chosen because each of them had several profiles nearby NAAMES cruise stations where ship-based ^{14}C NPP incubations were conducted, so that the performance of Argo float estimates of NPP could be evaluated. *Chl* was estimated from fluorometers on BGC-Argo floats, where the fluorometers were calibrated against discrete HPLC samples collected during NAAMES cruises. Float-measured particulate backscattering coefficients at 700 nm (bbp 700) were first converted to bbp at 470 nm using a power-law function with an exponent of 0.78 following Boss et al. (2013) and assuming the particulate backscattering ratio to be wavelength invariant. And then C_{phyto} was calculated using bbp 470 with the algorithm from Graff et al. (2015). It should be noted that a drawback of such approach is that a portion of the scattered light is due to non-algal particles. The floats operated with a profiling frequency from 1 to 5 days and had a depth resolution of ~2 m in the upper 500 m and ~4 m from 500 to 1,000 m. The BGC-Argo float data and documentation are available at <http://misclab.umeoce.maine.edu/floats/>.

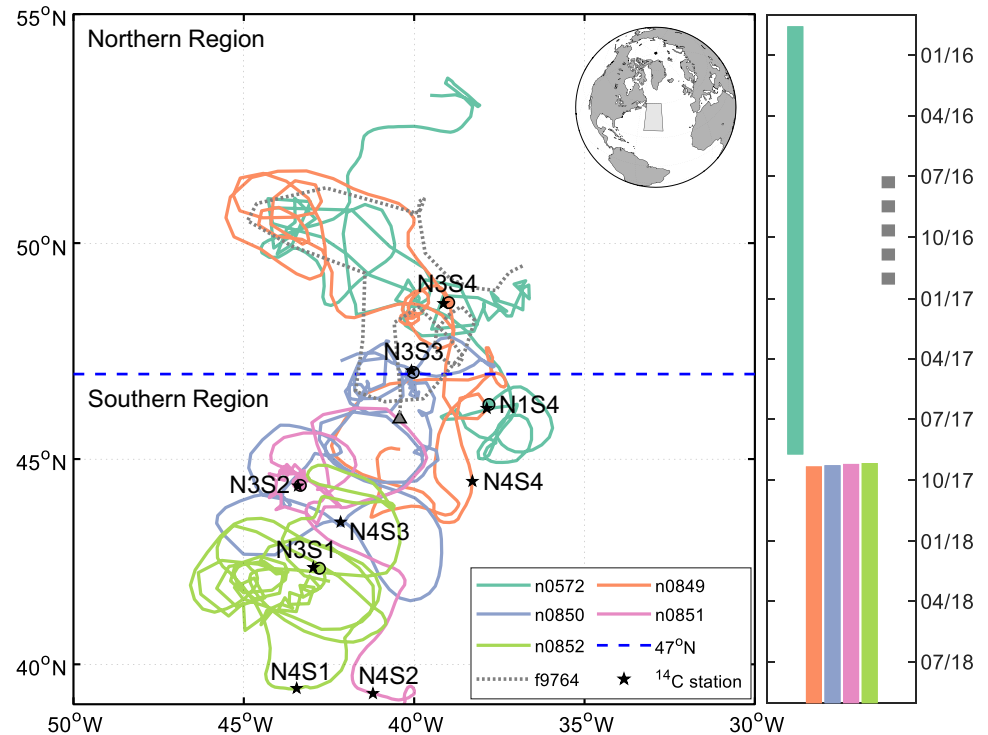


Figure 1. Trajectories of seven Argo profiling floats with the initial float deployment locations denoted by filled symbols. The bar chart (right panel) indicates float deployment durations. The dotted lines indicate the trajectory of SOS-Argo f9764 for NCP estimates, and all other floats are BGC-Argo for NPP estimates. SOS-Argo data are available at <https://sites.google.com/a/uw.edu/sosargo/home> and BGC-Argo data are available at <http://misclab.umeoce.maine.edu/floats/>. The dash-line at 47°N divided the research area into the northern (temperate) and southern (subtropical) regions. Stars (labeled with the station ID) indicate ship stations where ¹⁴C NPP values were measured during NAAMES cruises (Fox et al., 2020) and compared with NPP from nearby Argo floats. The circles and triangle indicate the locations where BGC-Argo and SOS-Argo were first deployed.

2.3. NPP Calculation

2.3.1. Carbon-Based Productivity Model (CbPM)

The first NPP model used in this study is the original CbPM model (Behrenfeld et al., 2005). In the CbPM, mixed layer NPP was calculated as the product of phytoplankton carbon (C_{phyto} , mg C m^{-3}) and phytoplankton specific growth rate (μ , d^{-1}) in the mixed layer:

$$NPP_{\text{mld}}^{\text{CbPM}} = C_{\text{phyto}} \cdot \mu \quad \text{mg C m}^{-3} \text{d}^{-1} \quad (1)$$

where μ was calculated using the equation modified CbPM (T. Westberry et al., 2008):

$$\mu = \frac{2 \cdot \text{Chl} / C_{\text{phyto}} \cdot (1 - \exp^{-5I_g})}{0.022 + (0.045 - 0.022) \cdot \exp^{-3I_g}} \quad \text{d}^{-1} \quad (2)$$

and where Chl is the chlorophyll concentration (mg m^{-3}), I_g is the median daily light level ($\text{mol photons m}^{-2} \text{h}^{-1}$) in the mixed layer. The value of I_g was estimated using satellite-derived surface photosynthetically active radiation (PAR) at the ocean surface (I_0) following:

$$I_g = I_0 \cdot \exp^{-K_{\text{PAR}} \cdot \text{MLD}/2} \quad \text{mol photon m}^{-2} \text{d}^{-1} \quad (3)$$

where the mixed layer depth (*MLD*) (m) was defined by a density offset from the value at 10 m with a threshold of 0.03 kg m^{-3} (deBoyer Montégut et al., 2004) using float-measured *S* and *T*. K_{PAR} is the diffuse attenuation coefficient of PAR, which was calculated using Equations 4a and 4b (Morel et al., 2007).

$$K_{PAR} = 0.0864 + 0.884 \cdot K_{490} - 0.00137 \cdot K_{490}^{-1}, \text{ when } MLD \leq K_{490}^{-1} \quad (4a)$$

$$K_{PAR} = 0.0665 + 0.874 \cdot K_{490} - 0.00121 \cdot K_{490}^{-1}, \text{ when } MLD > K_{490}^{-1} \quad (4b)$$

where K_{490} is the 490 nm diffuse attenuation coefficient (m^{-1}), calculated from float-measured *Chl-a* concentration (Morel & Maritorena, 2001):

$$k_{490} = 0.0166 + 0.07242 \cdot Chl^{0.68955} \text{ m}^{-1} \quad (5)$$

It should be noted that for depth-resolved NPP, the CbPM calculation was performed using the full Argo *Chl* and C_{phyto} profiles, and the actual light level at each depth (I_z).

$$I_z = I_0 \cdot \exp(-K_{PAR} \cdot Z) \text{ mol photon m}^{-2} \text{ d}^{-1} \quad (6)$$

2.3.2. Photoacclimation Productivity Model (PPM)

The second model used in this study is the Photoacclimation Productivity Model (PPM) developed during the NAAMES project (Fox et al., 2020). Similar to the CbPM, this second approach computes depth-resolved NPP using an estimate of phytoplankton growth rate and biomass (Equation 1), but it also uses the photoacclimation model of Behrenfeld et al. (2016) to account for nuances of chlorophyll synthesis caused by dynamic exposure to light and darkness in the mixed layer. Accordingly, μ was calculated as:

$$\mu = \left[\left(\frac{1}{\theta_{DM}} (-16.80) + 1.57 \right) \cdot \left(\frac{1}{\theta_{PaM}} (47.03) + 0.0125 \right) \right] \cdot \left[1 - e^{(-5 \cdot I_z)} \right] \text{ d}^{-1} \quad (7)$$

where θ_{DM} represents a deep-mixing term that accounts for molecular signals regulating chlorophyll synthesis during exposure to darkness, such that chlorophyll synthesis abates:

$$\theta_{DM} = 19 \cdot e^{\left(\frac{0.038 I_0^{0.45}}{k_{PAR}} \right)} \quad (8)$$

and θ_{PaM} implements a shallow-mixing correction for mixed layers less than 6 optical depths:

$$\theta_{PaM} = 19 \cdot e^{\left(\frac{0.038 I_0^{0.45}}{k_{PAR}} \right)} \cdot \frac{1 + e^{(-0.15 I_0)}}{1 + e^{(-3 I_g)}} \quad (9)$$

The PPM assumes that dark conditions occur at depths greater than 6 optical depths and that the value of θ_{PaM} for mixing depths greater than this horizon are described by θ_{DM} . For depths below the mixed layer the shallow-mixing term is not applied in the second component of Equation 7 (i.e., θ_{DM} is used instead of θ_{PaM}). The final term in Equation 7 describes the reduction in growth rate resulting from decreasing ambient light, which is estimated iteratively with depth. This decrease reflects the strength of the light limitation effect on μ and is characterized by the exponent (-5) (T. Westberry et al., 2008). As with the CbPM, I_z in Equations 7–9 is the PAR value at depth of *Z* (m), which was estimated from surface PAR using Equation 6.

2.4. Evaluation of Argo-Derived NPP With ^{14}C Incubation Result

Ship-based ^{14}C NPP incubation results are still the gold standard of NPP measurements in the field, recognizing that there might be some artifacts from ^{14}C incubation experiments (Morán et al., 2007; T. K. Westberry et al., 2012) as well as potential uncertainties here from the temporal/spatial mismatches of Argo and incubation data. The ^{14}C NPP data from nine stations (black stars in Figure 1) on three NAAMES cruises

were used to evaluate the performance of the bio-optical-measurement-based Argo NPP estimates. Evaluations are presented in the context of surface NPP (Section 3.1.1) and depth-resolved NPP (Section 3.1.2), respectively. When there were multiple Argo profiles during the same 24-h incubation experiment, the Argo-derived NPP values were averaged and then compared with the ^{14}C incubation result. Type II linear regression was used for the evaluation because both Argo-based NPP and ^{14}C -based NPP are measured parameters with uncertainties and dependent on the same environmental conditions and biological/physical processes.

NPP data from ^{14}C incubation experiments during NAAMES 1 to NAAMES 4 cruises (stations shown in Figure 1) are available at <https://seabass.gsfc.nasa.gov/experiment/NAAMES>.

In brief, water collected by Niskin bottles pre-dawn were spiked with ^{14}C -bicarbonate and incubated for 24 h (dawn-o-dawn) at different light levels (corresponding to the sample depth) in on-deck incubators to provide depth-resolved NPP [full details are provided in Fox *et al.* (2020)].

2.5. Auxiliary Data

For comparison purposes, satellite-based estimates of surface NPP were compiled from Moderate Resolution Imaging Spectroradiometer (MODIS) products (*Chl*, b_{bp} , *T*, *PAR*, <http://sites.science.oregonstate.edu/ocean.productivity/1080.by.2160.8day.inputData.php>) and using the same CbPM algorithm described in Section 2.3.1. The MODIS data set used here had a spatial resolution of 0.167° by 0.167° and a temporal resolution of 8 days. The *Chl* product was derived using the Garver-Siegel-Maritorena model (GSM) algorithm (Maritorena *et al.*, 2002). The gridded satellite product was interpolated to match the float data. A 1D interpolation in time was applied first to match the time steps of Argo measurements and then a 2D interpolation in space was applied to interpolate the gridded satellite data to the Argo location. We also used MODIS derived surface *PAR* as I_0 for Argo NPP calculations because there were no reliable Argo-based *PAR* data for NPP calculations. Monthly nitrate data used in our analysis was taken from a 1° gridded global nitrate field from the World Ocean Atlas 2013 (Garcia *et al.*, 2013), presented as the area mean of each region (northern region: $46\text{--}36^\circ\text{W}$, $47\text{--}54^\circ\text{N}$; southern region: $46\text{--}36^\circ\text{W}$, $39\text{--}47^\circ\text{N}$).

2.6. In Situ oxygen Measurement and NCP Calculation

Oxygen data from the five NAAMES BGC-Argo floats lacked sufficient in situ calibration to assure adequate accuracy required for air-sea gas calculations as the floats did not measure oxygen in air (Bittig *et al.*, 2018). Therefore, the oxygen data used for NCP calculations were obtained from a nearby Special Oxygen Sensor Argo float (9764, WMO number 5704770) (Figure 1), together with the corresponding salinity, temperature, and depth data. Only 6-months of data (from July to December 2016) were utilized for calculating NCP-to-NPP ratios, corresponding to when the trajectory of SOS-Argo f9764 was close to the BGC-Argo n0572. It should be noted that using NCP and NPP estimates from two different floats introduces more uncertainties (e.g., spatial offsets) into the NCP-to-NPP ratio estimate. Oxygen was measured using the air-calibrated Aanderaa optode O_2 sensors on the SOS-Argo float, with an accuracy better than $\pm 0.2\%$ (Bushinsky *et al.*, 2016). The profiling float operated at an interval of 5 days, covering depths from the surface to $\sim 1,900$ m. The vertical resolution in the top 200 m (where most of the carbon production occurs) was 3–5 m. The SOS-Argo float data are available at <https://sites.google.com/a/uw.edu/sosargo/home>.

NCP was calculated using a one-dimensional mixed layer O_2 mass-balance model, simplified from a multi-layer model used in our previous studies (Bushinsky & Emerson, 2015; Yang *et al.*, 2018, 2019). Briefly, the time rate of change in the mixed layer oxygen inventory ($dh[\text{O}_2]/dt$, $\text{mol O}_2 \text{ m}^{-2} \text{ d}^{-1}$, where h is the *MLD*) is the result of gas exchange (F_{A-W}), vertical advection (F_w), entrainment (F_E), diapycnal eddy diffusion (F_{Kz}) at the base of the mixed layer, and net biological oxygen production (F_{NCP}):

$$\frac{dh[\text{O}_2]}{dt} = F_{A-W} + F_w + F_E + F_{Kz} + F_{NCP} \text{ mmol m}^{-2} \text{ d}^{-1} \quad (10)$$

The net biological O_2 production (F_{NCP}) is evaluated as the difference between the measured O_2 time rate of change ($dh[\text{O}_2]/dt$) and the calculated fluxes (F_{A-W} , F_w , F_E and F_{Kz}), and then converted to carbon production

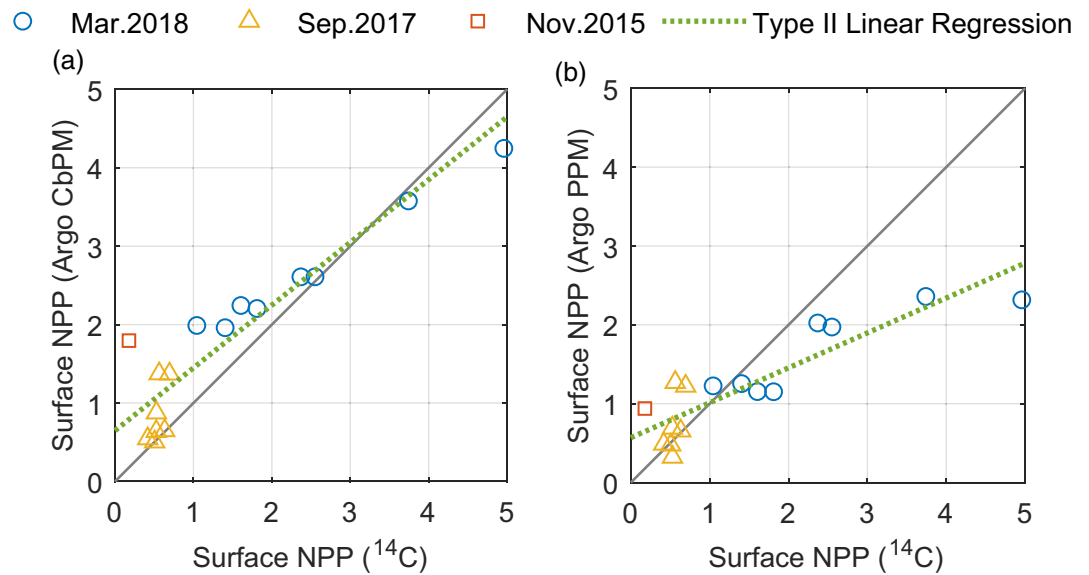


Figure 2. Comparison of surface net primary production (NPP, $\text{mmol m}^{-3} \text{d}^{-1}$) derived from ^{14}C approach and Argo estimates using CbPM (a) and PPM (b). The gray diagonal line is 1:1 line and the green dotted line presents Type II linear regression line. Type II linear regression result for CbPM: $y = (0.80 \pm 0.08)x + (0.65 \pm 0.16)$, $R = 0.93$, $\text{RMSD} = 0.41 \text{ mmol m}^{-3} \text{d}^{-1}$. Type II linear regression result for PPM: $y = (0.44 \pm 0.06)x + (0.57 \pm 0.11)$, $R = 0.88$, $\text{RMSD} = 0.29 \text{ mmol m}^{-3} \text{d}^{-1}$.

(NCP) with a constant oxygen to carbon molar ratio of 1.45 (Hedges et al., 2002). The dominant term in the oxygen mass balance (other than F_{NCP}) is the air-sea gas exchange ($F_{\text{A-W}}$), which was derived with the Argo-measured O_2 and satellite-measured wind speed (U_{10} , from the advanced scatterometer, ASCAT, <http://apdr.c.soest.hawaii.edu/las/v6/>) using an air-sea gas exchange model developed by Liang et al., (2013) and improved by Emerson et al. (2019).

3. Results and Discussion

3.1. Evaluation of Argo-Derived NPP

3.1.1. Evaluation of Surface NPP

For surface NPP comparisons, ^{14}C NPP data with sample/incubation depths shallower than 5 m were chosen and compared with the corresponding Argo NPP results. The CbPM model yielded surface NPP values close to the ^{14}C NPP values (Figure 2a, with the slope of type II regression = 0.80, $R = 0.93$, $\text{RMSD} = 0.41 \text{ mmol m}^{-3} \text{d}^{-1}$). The regression line for PPM NPP was further from the 1:1 line (gray solid line), with a slope of 0.44 (Figure 2b, $R = 0.88$, $\text{RMSD} = 0.29 \text{ mmol m}^{-3} \text{d}^{-1}$).

3.1.2. Evaluation of Depth-Resolved NPP

The comparison between CbPM-based (depth-resolved) Argo NPP and ^{14}C NPP is presented in Figures 3a-3i. A type II linear regression (Figure 3j, the green dotted line) showed good agreement between the CbPM-based Argo approach and ^{14}C measurements of depth-resolved NPP ($R = 0.90$, $\text{RMSD} = 0.51 \text{ mmol m}^{-3} \text{d}^{-1}$), and the slope of 0.99 showed that the CbPM model performed well in reproducing the magnitude of NPP. The largest discrepancy between the ^{14}C NPP and CbPM-based Argo NPP occurred at mid-depths during the NAAMES 3 cruise (September 2017, yellow triangles in Figure 3j). The middepth NPP maximum indicated by the Argo data (also consistent with the middepth *Chl-a* maximum, Figure S6) was not found in most of the ^{14}C incubation profiles (except for the slightly elevated NPP at N3S2 around 50 m, see below), the most likely explanation for such a mismatch being elevated chlorophyll levels from subsurface photoacclimation. In the summer or early fall when surface and upper-ocean light intensity is high, phytoplankton decrease the concentration of light-harvesting pigments such as chlorophyll a, while the same pigments increase at middepth as the light level decreases. This cellular process likely causes the subsurface peak of

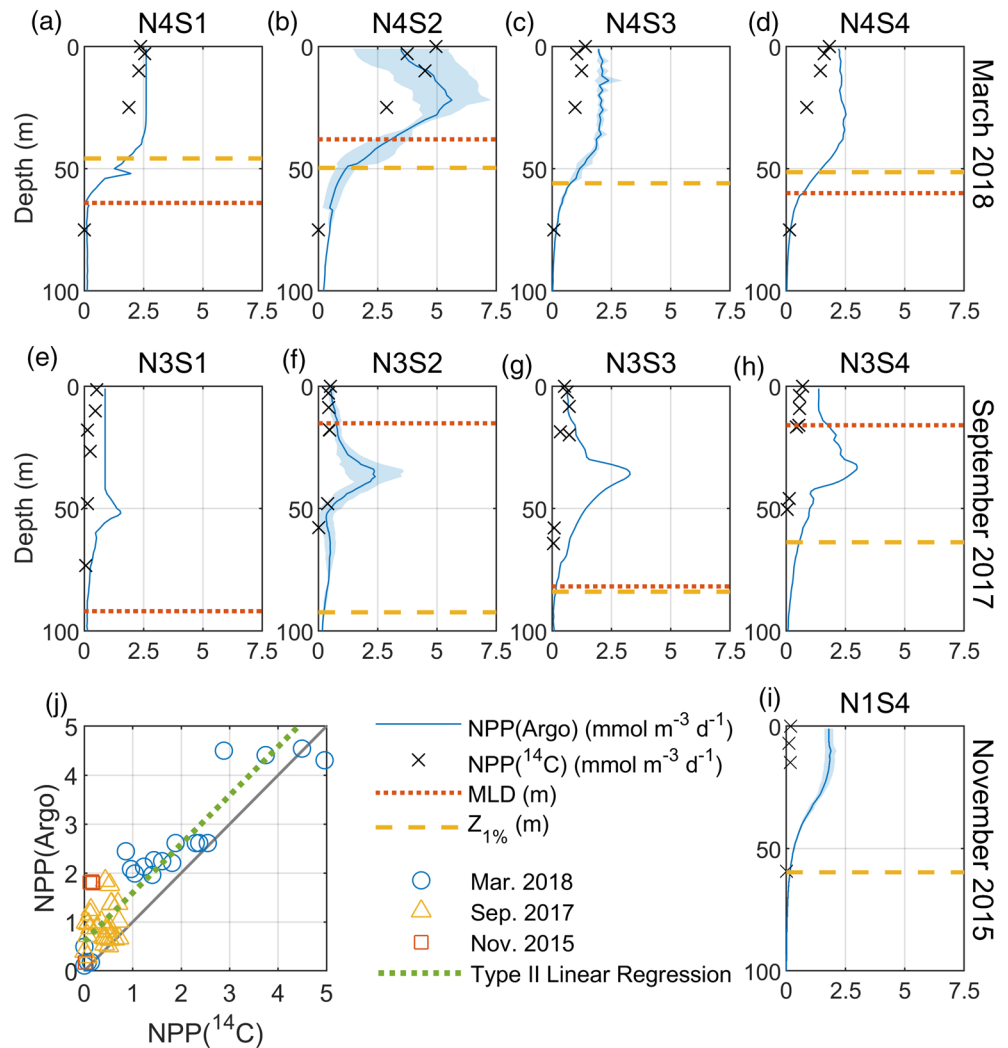


Figure 3. (a–i) Net primary production (NPP, $\text{mmol m}^{-3} \text{d}^{-1}$) profiles derived from BGC-Argo floats (blue line) on NAAMES ^{14}C stations, using the Carbon-based Productivity Model (CbPM). Black “x” indicates NPP results from onboard ^{14}C incubation experiments during NAAMES1 to NAAMES4 cruises (Fox et al., 2020). The blue shading indicates the standard deviation of multiple Argo profiles during the same 24-h incubation experiment. The red dotted line and yellow dash line indicate mixed layer depth (MLD, m) and euphotic depth ($Z_{1\%}$, m), respectively. (j) The correlation between NPP estimates from Argo and ^{14}C measurements. The gray diagonal line in the background is the 1:1 line. The green dotted line is from a type II regression: $y = (0.99 \pm 0.07)x + (0.60 \pm 0.10)$, $R = 0.90$, $\text{RMSD} = 0.51 \text{ mmol m}^{-3} \text{d}^{-1}$.

Chl-a (Figure S6) observed in the September 2017 data. Because the CbPM model has limited capacity to account for photoacclimation below the MLD, the subsurface peak of *Chl-a* also led to artifacts of subsurface maximum in NPP (Figures 3e–3h).

The comparison between PPM-based (depth-resolved) Argo NPP and ^{14}C NPP is presented in Figures 4a–4i. The correlation coefficient R and RMSD for PPM-based NPP were 0.81 and $0.37 \text{ mmol m}^{-3} \text{d}^{-1}$, respectively (Figure 4j). However, compared to the CbPM approach, the regression line (green dotted line in Figure 4j) between depth-resolved PPM-based NPP and ^{14}C was also further from the 1:1 line, with a slope of 0.50 (similar to the regression result in the surface: slope = 0.44, Figure 2b). There are several possible explanations for the underestimated NPP from PPM-based Argo approach. First, it is possible that the above mentioned temporal/spatial mismatches of the Argo and cruise data and the potential artifacts from ^{14}C incubation affected the comparison of ^{14}C -based NPP and CbPM/PPM-based NPP. Second, the PPM algorithm used for Argo NPP calculation might have some systematic biases that are not, as of yet, fully understood. The PPM

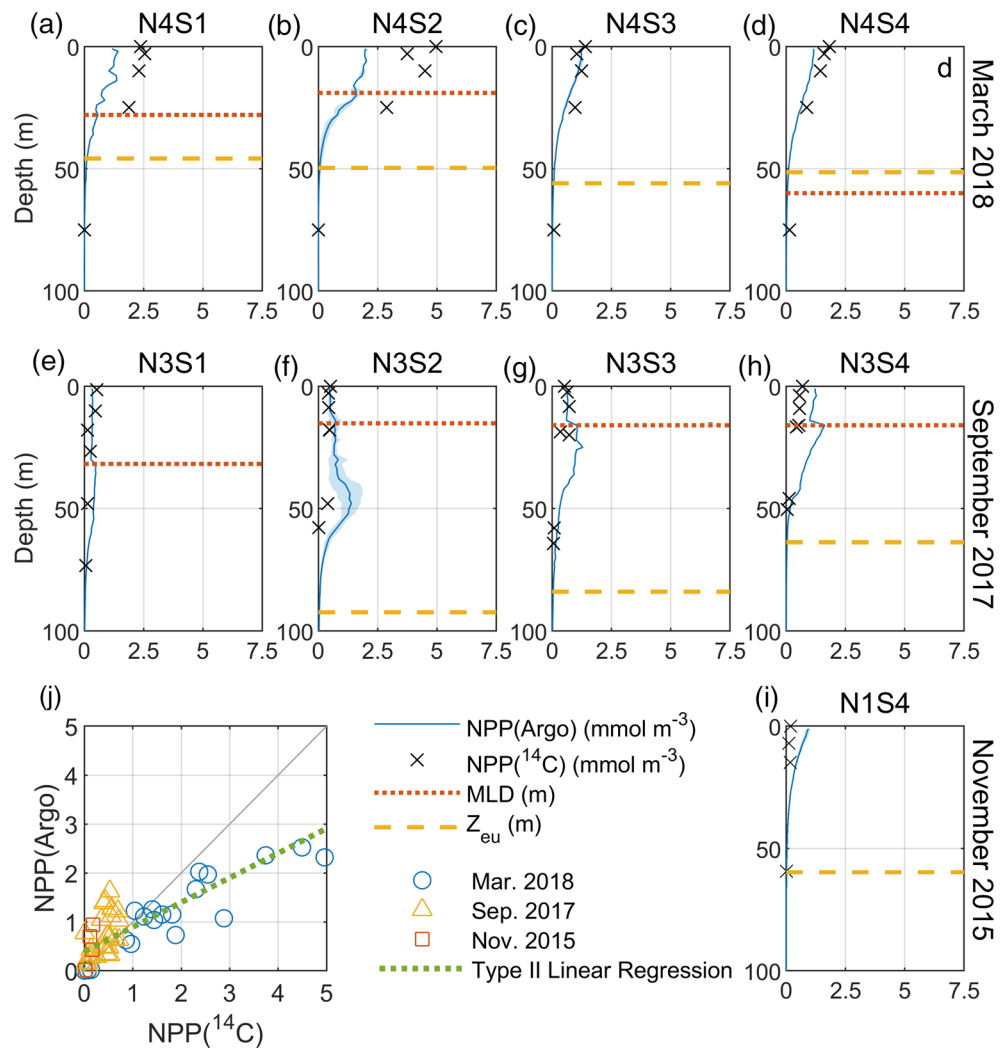


Figure 4. (a–i) Net primary production (NPP, $\text{mmol m}^{-3} \text{d}^{-1}$) profiles derived from BGC-Argo floats (blue line) on NAAMES ^{14}C stations, using the PPM model from Fox *et al.*, (2020). Black “x” indicates NPP results from onboard ^{14}C incubation experiments during NAAMES1 to NAAMES4 cruises (Fox *et al.*, 2020). The blue shading indicates the standard deviation of multiple Argo profiles during the same 24-h incubation experiment. The red dotted line and yellow dash line indicate mixed layer depth (MLD, m) and euphotic depth ($Z_{1\%}$, m), respectively. (j) The correlation between NPP estimates from Argo and ^{14}C measurements. The gray diagonal line in the background is the 1:1 line. The green dotted line is from a type II regression with all data: $y = (0.50 \pm 0.05)x + (0.39 \pm 0.07)$, $R = 0.81$, $\text{RMSE} = 0.37 \text{ mmol m}^{-3} \text{d}^{-1}$.

model used modeled θ_{PAM} rather than the measured Chl/C used in CbPM. Therefore, the PPM model is less vulnerable to the high Chl/C caused by photoacclimation during the summer months. As a result, the PPM-based Argo NPP did not have any large subsurface NPP maximum for the NAAMES 3 cruise in September 2017 (Figures 4e–4h). However, the PPM result did show slightly elevated subsurface NPP (N3S1 near 30 m, N3S2 near 40 m, N3S3 and N3S4 near 20 m), which was also captured by ^{14}C NPP profiles (i.e., N3S2 and N3S3, Figures 4f and 4g) and was most likely due to the surface nutrient depletion (Figures S7e–S7h).

Overall, our analysis showed that both the CbPM and PPM models generally performed well in reproducing the NAAMES NPP data estimated with the state-of-the-art ^{14}C incubation-based NPP measurements, with their own advantages and limitations. The CbPM model reproduced the magnitude of NPP but had some artifacts when subsurface photoacclimation was significant. The PPM model accounts for effects of subsurface photoacclimation, but the model-estimated NPP was much lower than the ^{14}C NPP estimates. Our result indicates that it is critical to choose an appropriate model for Argo-based NPP calculations under

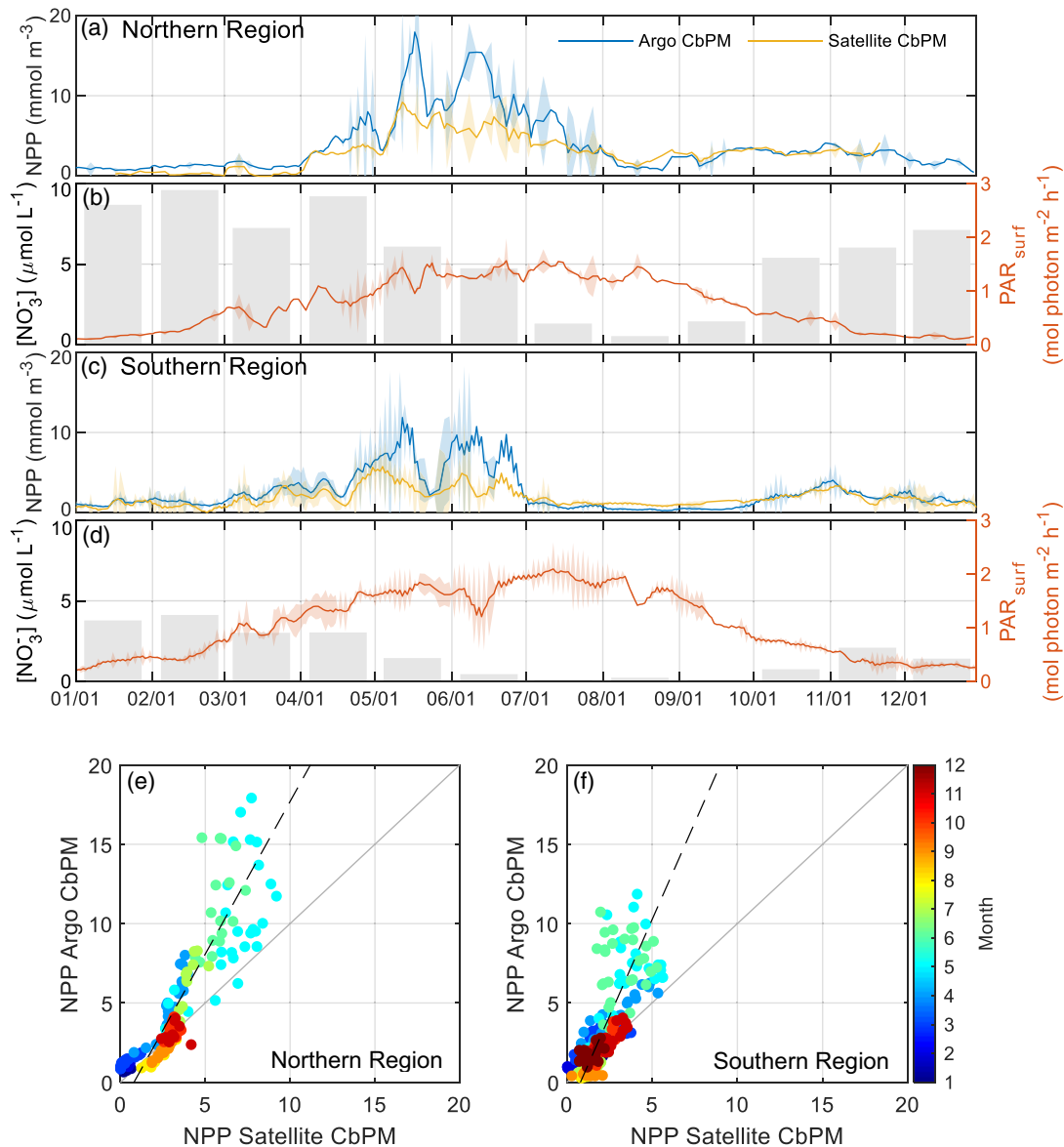


Figure 5. Climatologies of surface net primary production (NPP) for the northern region (a) and southern region (c) from Argo (blue line) and Satellite (yellow line) using CbPM model. Panels (b and d) show surface photosynthetically active radiation (PAR_{surf} , red line) and the monthly climatology of surface nitrate concentration ($[NO_3^-]$, gray bar) from World Ocean Atlas 2013 (Garcia et al., 2013). The shadings in panels (a–d) indicate one standard deviation. Correlation analysis of panels (a and c) are presented in panels (e–f) with the gray diagonal line as 1:1 line and the black dash line as type II regression line. Type II linear regression result for Northern Region: $y = (1.92 \pm 0.08)x + (-1.53 \pm 0.28)$, $R = 0.88$, $RMSD = 2.02 \text{ mmol m}^{-3} \text{ d}^{-1}$. Type II linear regression result for Southern Region: $y = (2.44 \pm 0.10)x + (-1.95 \pm 0.21)$, $R = 0.79$, $RMSD = 1.74 \text{ mmol m}^{-3} \text{ d}^{-1}$.

different circumstances and that more efforts need to be invested to improve NPP estimates from bio-optical measurements from profiling floats.

3.2. Spatial and Temporal Distribution of NPP in the Western North Atlantic

3.2.1. Spatial and Temporal Distribution of Surface NPP

First, we analyzed the spatial and temporal distribution of NPP in the western North Atlantic in the context of an annual climatology of surface NPP derived from Argo float data. The Argo results from the CbPM model (blue line in Figures 5a and 5c) were used here, because our evaluation showed no artifacts of

photoacclimation in the surface NPP with the CbPM model and the magnitude of NPP from CbPM model agreed better with the ^{14}C NPP results.

For the northern region (Figure 5a), NPP was low ($\sim 1 \text{ mmol m}^{-3} \text{ d}^{-1}$) for the first 3 months of the year (January–March), due to the lower light level (red line, Figure 5b) in the wintertime. Phytoplankton concentrations notably increased from April forward, with NPP increasing substantially through the spring and summer, reaching the peak of $17 \text{ mmol m}^{-3} \text{ d}^{-1}$ in mid-May. By mid-June, NPP started decreasing toward a relatively low value around $1.3 \text{ mmol m}^{-3} \text{ d}^{-1}$ in mid-August, which could have been due to nutrient limitation (gray bar in Figure 5b), and over-grazing. These factors could also have explained the increasing NPP after mid-August and a plateau with NPP of $3 \text{ mmol m}^{-3} \text{ d}^{-1}$ observed from late September to late November, as the increasing *MLD* could have helped relieve stresses from nutrient limitation (by mixing with nutrient-rich deep water) and grazing (by reducing the encounter rate of phytoplankton and grazers). After late November, with worsening light condition, NPP decreased fast and reached near-zero values by the end of the year, which aligned well with the observations in January. Overall, this seasonal pattern of NPP was consistent with the phytoplankton phenology reported in our previous work (Yang et al., 2020) and can be explained by the disturbance recovery hypothesis (DRH, (Behrenfeld & Boss, 2018)).

For the southern region, the overall seasonal pattern was similar but with several distinct characteristics (Figure 5c). First, the timing for each stage of the NPP phenology was different. In the southern region, the significant increase in NPP started in March (Figure 5c), about 1 month earlier than that in the northern region (Figure 5a), which could be related to the better light condition. On the other hand, after the summer peak, NPP quickly dropped below 1 mmol m^{-3} by the end of June in the southern region as surface nutrients were quickly depleted (Figure 5d), indicating that the difference in nutrient supply of the Northern and Southern Regions is also an important factor that controls phytoplankton phenology. The low NPP values continued until late September (much longer than that in the northern region), consistent with the depleted nutrients shown in Figure 5d and indicating that nutrient limitation may have played a more important role in the southern region. Second, NPP in January and February was higher in the southern region, because the light condition was better at lower latitude in the winter (Figures 5b and 5d).

On the other hand, the summer NPP maximum ($\sim 10 \text{ mmol m}^{-3} \text{ d}^{-1}$) was lower in the southern region than in the northern region. Surface PAR at the southern region NPP climax (close to $2 \text{ mol photon m}^{-2} \text{ h}^{-1}$, Figure 5d) was higher than that of the northern region NPP climax (below $1.5 \text{ mol photon m}^{-2} \text{ h}^{-1}$, Figure 5b). Based on climatology, surface nutrient levels were low, but not zero, during the climax for the southern region (Figure 5d). A possible explanation for the lower NPP climax levels in the southern region is that the southern region has a weaker over all bloom, due to the lower wintertime nutrient supply or summer macro- or micro-nutrient limitation. Although NPP from October to January was slightly lower in the southern region than that in the northern region, it actually represented a larger contribution to annual production, since the summer NPP in the southern region was not as high as that in the northern region.

NPP estimates from satellite-based *Chl* and C_{phyto} (yellow line in Figures 5a and 5c) were also compared to the Argo float results. For most of a year, the Argo and satellite estimates of NPP were comparable. The largest differences occurred in the late spring and summer months when NPP was high (Figures 5e and 5f), consistent with the fact that the Argo estimates of *Chl* and C_{phyto} were also higher than satellite estimated for those months (Figure S8). Such mismatch could be the result of spatial/temporal mismatch of Argo and satellite data and/or the systematic offsets between the Argo and satellite measurements.

3.2.2. Spatial and Temporal Distribution of Depth-Resolved NPP

For the analysis of depth-resolved NPP, we present monthly climatologies of NPP from the PPM model (Figure 6) because the PPM model did not have photoacclimation-related artifacts (large subsurface NPP peak) in the summer. Although the NPP from the PPM model might have underestimated the magnitude of NPP (as shown in section 3.1.2), this bias should not affect the analysis on seasonal NPP variations. Monthly climatologies of nitrate concentration ($[\text{NO}_3^-]$, Figure 8) and PAR (Figure 7) were also created to help with our analysis.

For the northern region (Figure 6, upper panel), the NPP profiles showed an exponential-like shape with NPP decreasing with depth, similar to the PAR profiles (Figure 7, upper panel). Such patterns indicate that

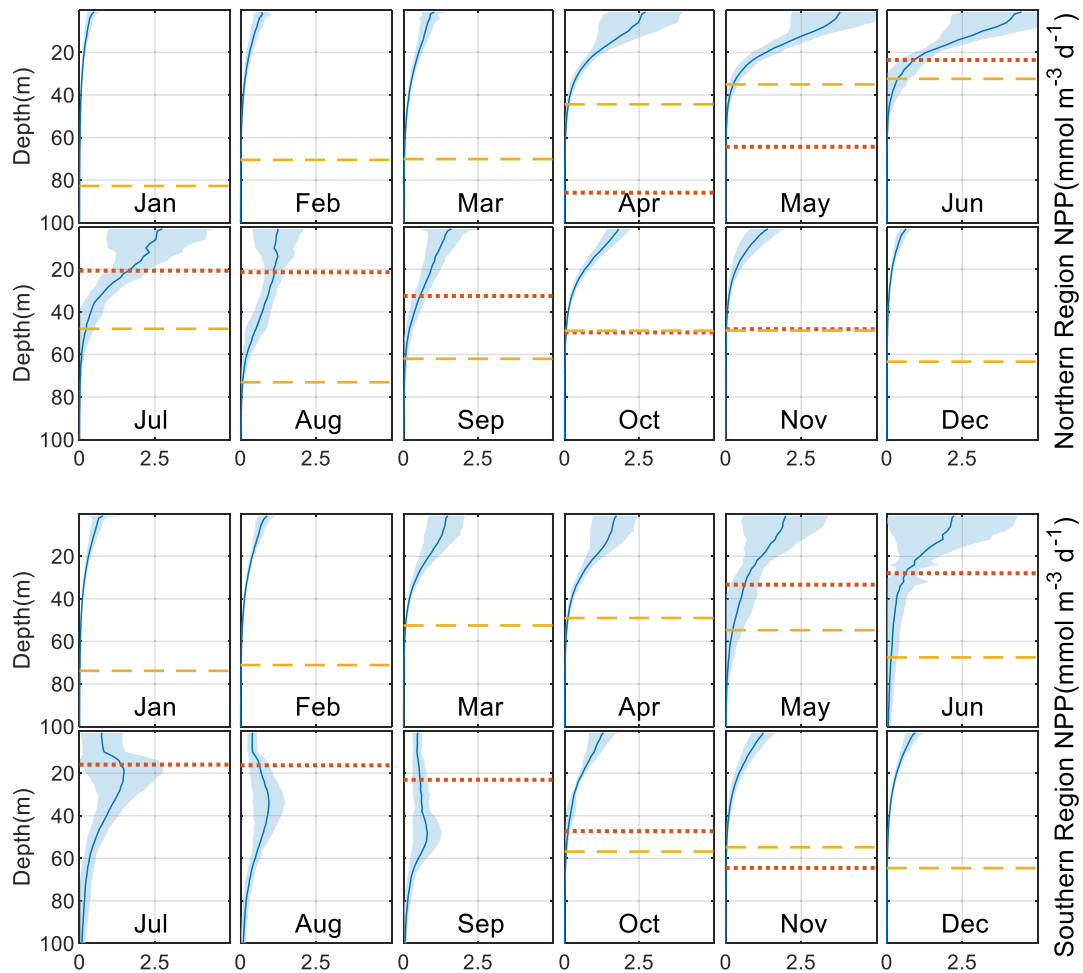


Figure 6. Monthly climatologies of net primary production (NPP, $\text{mmol m}^{-3} \text{d}^{-1}$) profiles derived from BGC-Argo measurements using the PPM model from Fox et al. (2020). The shadings indicate one standard deviation. The red dotted line and yellow dash line indicate mixed layer depth (MLD, m) and euphotic depth ($Z_{1\%}$, m), respectively.

the light condition was likely the major control of NPP distributions at depth in the northern region. The seasonal pattern of depth-resolved NPP in the northern region was similar to the seasonal pattern of surface NPP (Figure 5a), with NPP increasing from spring to summer, NPP climax in June, low NPP in August, a second NPP peak in September and October, and decreasing NPP in November and December.

For the southern region, the seasonal pattern of depth-resolved NPP (Figure 6, lower panel) was also similar to the seasonal pattern of the surface NPP (Figure 5c). For most of the year, the depth distribution of NPP in the southern region also followed an exponential-like pattern similar to the PAR distribution, with the exception in the summer months (July, August, and September). For these 3 summer months, the NPP profile was almost a straight line from the surface to 15–40 m and was far from the exponential-like pattern of PAR (Figure 7), indicating that the light condition was not the sole control of such NPP depth distribution. On the other hand, nitrate was depleted from the surface to about 20 m and started increasing below 20 m (Figure 8), which likely explained the low NPP in the shallow water, and the slightly elevated subsurface NPP observed by Argo float (July to September, lower panel of Figure 6) and the ^{14}C result from NAAMES 3 (i.e., N3S2 and N3S3, Figures 4f and 4g). Overall, the depth-resolved NPP revealed similar differences between the northern and southern region as suggested by the surface NPP, including the higher winter NPP/lower summer NPP in the south, and timing difference in NPP phenology. The more nutrient-controlled NPP depth distribution in the southern region for summer months was distinct from the more light-controlled NPP depth distribution in the north.

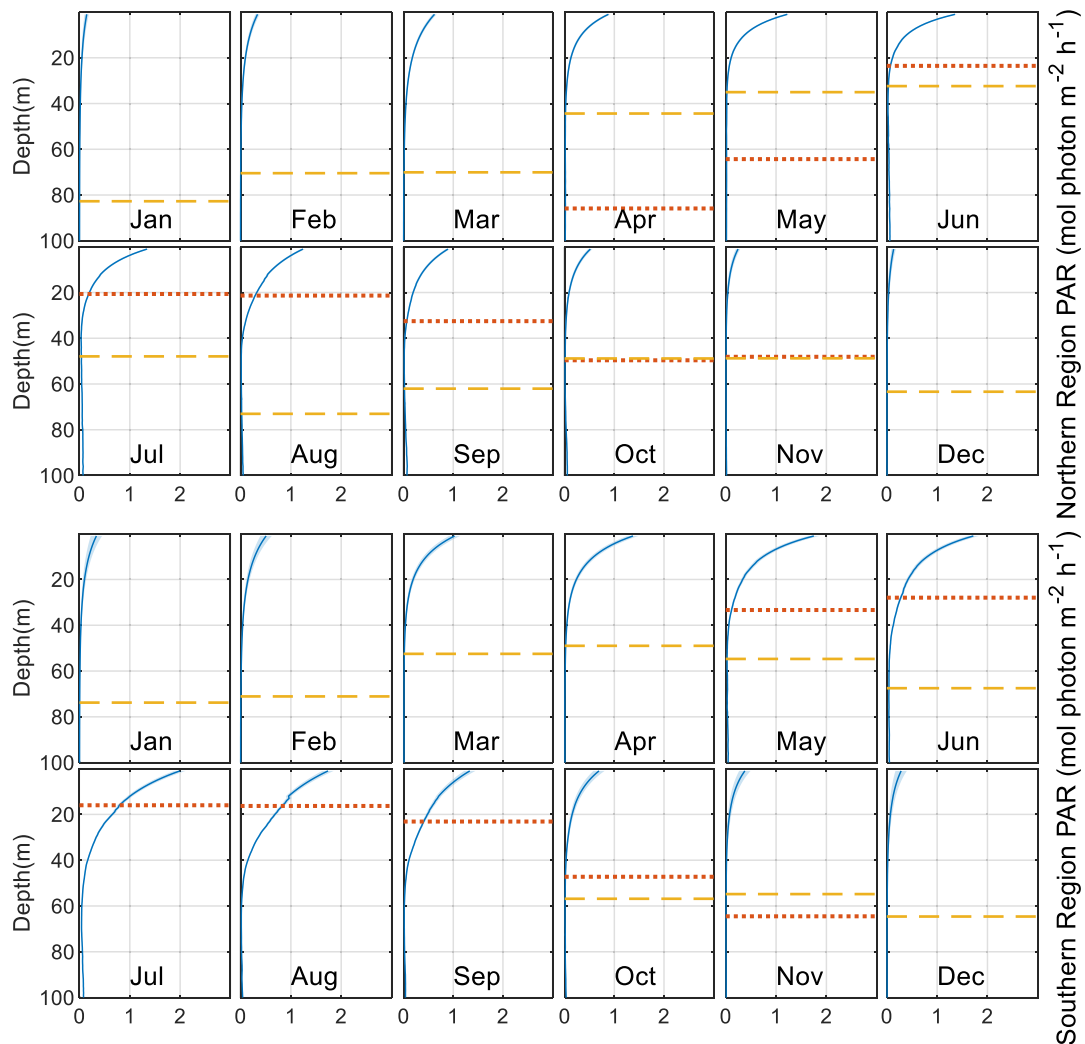


Figure 7. Monthly climatologies of photosynthetically active radiation (PAR, mol photon $\text{m}^{-2} \text{h}^{-1}$) profiles derived from Satellite data (<http://sites.science.oregonstate.edu/ocean.productivity/1080.by.2160.8day.inputData.php>). The shadings indicate one standard deviation. The red dotted line and yellow dash line indicate mixed layer depth (MLD, m) and euphotic depth ($Z_{1\%}$, m), respectively.

Comparison was also made with previous Argo NPP study in the North Atlantic (Briggs et al., 2018). Although their research area was about 4–8° north to our northern-most location, the magnitude of observed NPP values were comparable. Their study yielded an integrated NPP (surface to 60 m) of $\sim 84 \text{ mmol C m}^{-2} \text{ d}^{-1}$ during the spring bloom in an area from 58°N to 62°N (Briggs et al., 2018), while our corresponding results in the upper 60 m during the bloom period were $95 \text{ mmol C m}^{-2} \text{ d}^{-1}$ (northern region, 47°N to 54°N) and $73 \text{ mmol C m}^{-2} \text{ d}^{-1}$ (southern region, 39°N to 47°N), respectively.

3.3. Estimate of Mixed Layer NCP to NPP Ratio

In steady state, the NCP to NPP ratio is equivalent to the f-ratio (the amount of biologically produced carbon available for export) (Eppley & Peterson, 1979), which is a useful metric for quantifying the strength of the biological carbon pump. The most widely used estimates of the f-ratio are derived from an empirical relationship with temperature (Laws et al., 2000, 2011). However, these empirical equations are limited by the spatial and temporal coverages of field-observed f-ratios. In this study, we demonstrate the ability of Argo profiling floats in measuring f-ratios over large temporal and spatial scales by using concurrent measurements of NCP and NPP on two Argo floats (BGC-Argo n0572 and SOS-Argo f9764) from July to late

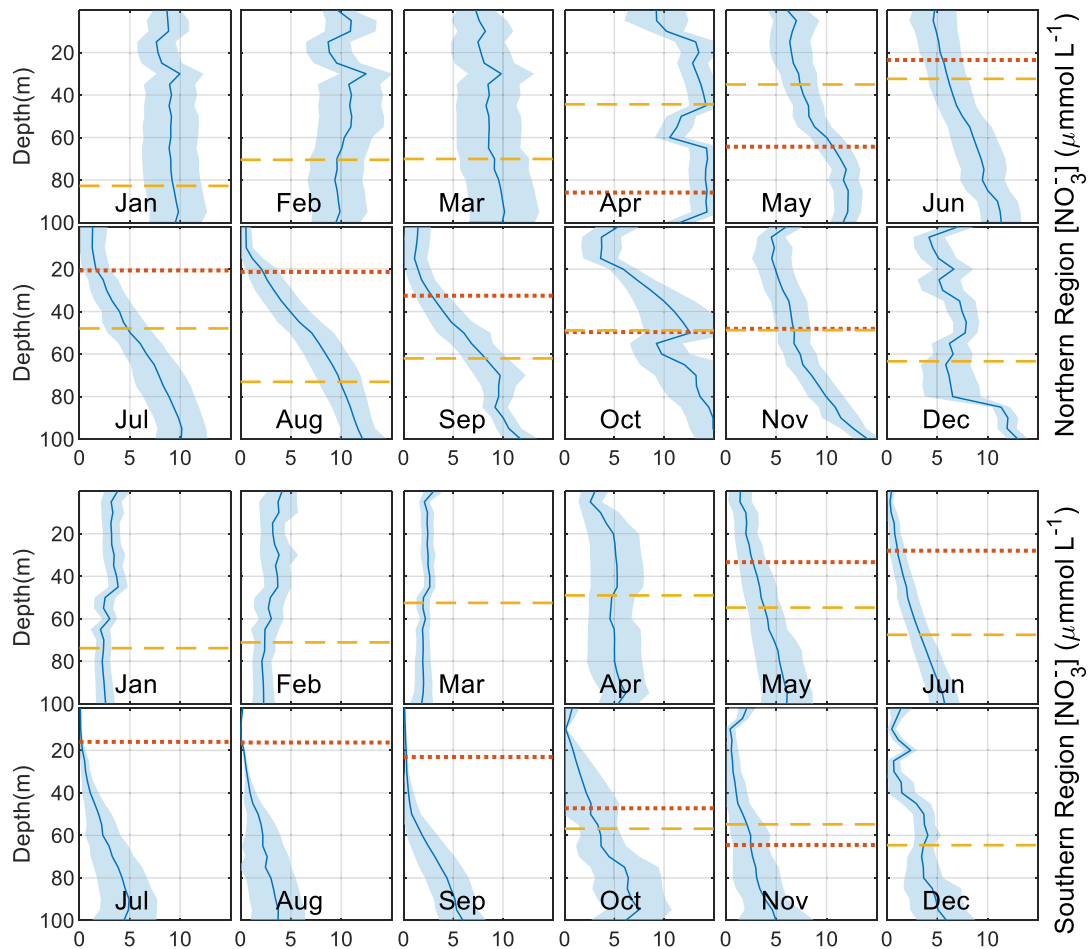


Figure 8. Monthly climatologies of nitrate ($[\text{NO}_3^-]$, $\mu\text{mol L}^{-1}$) profiles derived from World Ocean Atlas 2013. The shadings indicate one standard deviation. The red dotted line and yellow dash line indicate mixed layer depth (MLD, m) and euphotic depth ($Z_{1\%}$, m), respectively.

December of 2016. Although the distance between these two floats were not ideal (Figure S10), they roughly covered the same area (Figure 1) during this period of time and could give us a big picture of NCP to NPP ratio in this area. The mixed layer-integrated NCP (unit: $\text{mmol m}^{-2} \text{d}^{-1}$) from Equation 10 was converted to mixed layer mean NCP (unit: $\text{mmol m}^{-3} \text{d}^{-1}$). As shown in Figure 9a, the MLDs (determined from salinity and temperature, see the T-S plot in the supporting information) from these two floats were similar (except for September), indicating they were measuring the same water mass and therefore that it was reasonable to combine the NPP and NCP results from these two floats (Figure 9b) to estimate NCP/NPP ratios. For these months, NPP decreased sharply from July to mid-August and then increased slightly with a small peak in early September. Thereafter, NPP slowly decreased until late December. The NCP trend generally followed the NPP variations, except for July. The highest NCP/NPP ratio occurred between late August and early October, with peak values of 0.3. For comparison, a higher NCP/NPP value (0.3–0.7) was observed by Alkire et al. (2012) in the subarctic North Atlantic during the bloom season (April and May). NCP and the NCP/NPP ratio turned negative in mid-October and continued decreasing, with the lowest NCP/NPP values around -1.0 in December when both NPP and NCP were small. The negative winter NCP may reflect ventilation of low O_2 water and net respiration that occurred earlier in the shallow aphotic zone over the prior stratified season. Despite the potential spatial offsets between the two floats and temporal offset between NPP and NCP (NPP is instantaneous while NCP reflects the situation of several weeks prior in the mixed layer and longer in stratified subsurface waters), the Argo results clearly show significant seasonal variations in NCP/NPP ratios that are quite different than those derived from a traditional temperature-based empirical equation (purple line in Figure 9c, calculated with Equation 3 in Laws et al. [2011]).

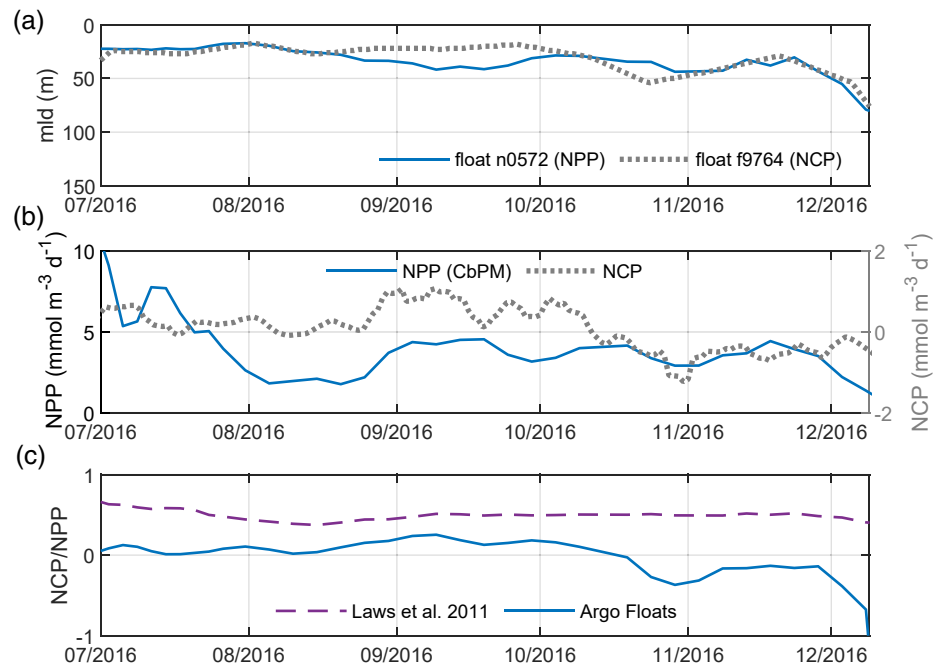


Figure 9. (a) Mixed layer depth from floats n0572 and f9764. (b) Mixed layer mean net primary production (NPP) and net community production (NCP). (c) Mixed layer mean NCP to NPP ratio (NCP/NPP). The purple dashed line indicates the NCP/NPP derived using temperature-based empirical algorithm (Equation 3 in Laws et al., 2011). NPP was derived from BGC-Argo n0572 using the Carbon-based Productivity Model (CbPM, Westberry et al., 2008). NCP was calculated from oxygen mass balance using data from SOS-Argo float f9764. Both NCP and NPP were converted to the mix layer mean (unit: $\text{mmol C m}^{-3} \text{d}^{-1}$).

4. Summary and Implications

In this study, we obtained for the first time year-round, in situ estimates of NPP in the western North Atlantic Ocean (39°N to 55°N , 30°W to 50°W) using the bio-optical measurements on BGC-Argo floats from the NAAMES project. The BGC-Argo-measured NPP was comparable and complementary to discrete-sampling-based ^{14}C incubation measurements, but it also filled the niche of temporal and spatial (both horizontally and vertically) coverage limitations of the ship-based ^{14}C and satellite remote sensing approaches. Evaluations against ^{14}C NPP incubation measurements showed advantages and limitations of both the CbPM and PPM bio-optical models. Specifically, the CbPM reproduced the magnitude of NPP in most cases (except those when subsurface photoacclimation was important), while PPM accounted for the effects of subsurface photoacclimation but overall was biased low compared to ^{14}C data. Overall, our work demonstrates that Argo float data provides an important, complementary approach to ^{14}C and satellite remote sensing estimates of NPP, with the potential to provide more information on the temporal and spatial distribution of phytoplankton carbon production. Our work also shows the limitations of current NPP models, and emphasizes the need for improving the NPP estimates using bio-optical measurements from Argo profiling floats.

Data Availability Statement

The Argo Program is part of the Global Ocean Observing System. These data were collected and made freely available by the International Argo Program and the national programs that contribute to it (<http://www.argo.ucsd.edu>, <http://argo.jcommops.org>). In addition to the links included in the main text (<http://misc-lab.umeoce.maine.edu/floats/>, <https://sites.google.com/a/uw.edu/sosargo/home>), the Argo data can also be obtained with WMO number at <http://www.argodatamgt.org/Access-to-data/Description-of-all-floats2>. Satellite-based Chl , b_{bp} , T , PAR can be obtained at: <http://sites.science.oregonstate.edu/ocean.productivity/1080.by.2160.8day.inputData.php>. U_{10} data is obtained from <http://apdrc.soest.hawaii.edu/las/v6/>.

Acknowledgments

Support for this work came from the National Aeronautics and Space Administration (NASA) as part of the North Atlantic Aerosol and Marine Ecosystems Study (NAAMES, grants 80NSSC18K0018).

References

- Alkire, M. B., D'Asaro, E., Lee, C., Perry, M. J., Gray, A., Cetinić, I., et al. (2012). Estimates of net community production and export using high-resolution, Lagrangian measurements of O_2 , NO_3^- , and POC through the evolution of a spring diatom bloom in the North Atlantic. *Deep Research Part I Oceanography Research Paper*, 64, 157–174. <https://doi.org/10.1016/j.dsr.2012.01.012>
- Behrenfeld, M. J., & Boss, E. S. (2018). Student's tutorial on bloom hypotheses in the context of phytoplankton annual cycles. *Global Change Biology*, 24(1), 55–77. <https://doi.org/10.1111/gcb.13858>
- Behrenfeld, M. J., Boss, E., Siegel, D. A., & Shea, D. M. (2005). Carbon-based ocean productivity and phytoplankton physiology from space. *Global Biogeochemical Cycles*, 19(1). <https://doi.org/10.1029/2004GB002299>
- Behrenfeld, M. J., Moore, R. H., Hostetler, C. A., Graff, J., Gaube, P., Russell, L. M., et al. (2019). The North Atlantic Aerosol and Marine Ecosystem Study (NAAMES): Science Motive and Mission Overview. *Frontiers Marine Science*, 6, 122. <https://doi.org/10.3389/fmars.2019.00122>
- Behrenfeld, M. J., & Falkowski, P. G. (1997). Photosynthetic rates derived from satellite-based chlorophyll concentration. *Limnology & Oceanography*, 42(1), 1–20. <https://doi.org/10.4319/lo.1997.42.1.0001>
- Behrenfeld, M. J., O'Malley, R. T., Boss, E. S., Westberry, T. K., Graff, J. R., Halsey, K. H., et al. (2016). Reevaluating ocean warming impacts on global phytoplankton. *Nature Climate Change*, 6(3), 323.
- Bittig, H. C., Körtzinger, A., Neill, C., van Ooijen, E., Plant, J. N., Hahn, J., , & (2018). Oxygen Optode Sensors: Principle, Characterization, Calibration, and Application in the Ocean. *Frontiers Marine Science*, 4, 429. <https://doi.org/10.3389/fmars.2017.00429>
- Boss, E., Picheral, M., Leeuw, T., Chase, A., Karsenti, E., Gorsky, G., et al. (2013). The characteristics of particulate absorption, scattering and attenuation coefficients in the surface ocean; Contribution of the Tara Oceans expedition. *Methods Oceanogr*, 7, 52–62. <https://doi.org/10.1016/j.mio.2013.11.002>
- Briggs, N., Guemundsson, K., Cetinić, I., D'Asaro, E., Rehm, E., Lee, C., & Perry, M. J. (2018). A multi-method autonomous assessment of primary productivity and export efficiency in the springtime North Atlantic. *Biogeosciences*, 15, 4515–4532. <https://doi.org/10.5194/bg-15-4515-2018>
- Burt, W. J., Westberry, T. K., Behrenfeld, M. J., Zeng, C., Izett, R. W., & Tortell, P. D. (2018). Carbon: Chlorophyll ratios and net primary productivity of subarctic Pacific surface waters derived from autonomous shipboard sensors. *Global Biogeochemical Cycles*, 32(2), 267–288. <https://doi.org/10.1002/2017GB005783>
- Bushinsky, S. M., & Emerson, S. (2015). Marine biological production from in situ oxygen measurements on a profiling float in the subtropical Pacific Ocean. *Global Biogeochemical Cycles*, 29(12), 2050–2060. <https://doi.org/10.1002/2015GB005251>
- Bushinsky, S. M., Emerson, S. R., Riser, S. C., & Swift, D. D. (2016). Accurate oxygen measurements on modified Argo floats using in situ air calibrations. *Limnology and Oceanography: Methods*, 14, 491–505. <https://doi.org/10.1002/lom3.10107>
- deBoyer Montégut, C., Madec, G., Fischer, A. S., Lazar, A., & Ludicone, D. (2004). Mixed layer depth over the global ocean: An examination of profile data and a profile-based climatology. *Journal of Geophysical Research*, 109(C12), C12003. <https://doi.org/10.1029/2004JC002378>
- Della Penna, A., & Gaube, P. (2019). Overview of (Sub)mesoscale Ocean Dynamics for the NAAMES Field Program. *Frontiers Marine Science*, 6, 384. <https://doi.org/10.3389/fmars.2019.00384>
- Emerson, S., Yang, B., White, M., & Cronin, M. (2019). Air-sea gas transfer: determining bubble fluxes with in situ N_2 observations. *Journal of Geophysical Research: Ocean*, 124, 2716–2727. <https://doi.org/10.1029/2018JC014786>
- Eppley, R. W., & Peterson, B. J. (1979). Particulate organic matter flux and planktonic new production in the deep ocean. *Nature*, 282(5740), 677–680. <https://doi.org/10.1038/282677a0>
- Estapa, M. L., Feen, M. L., & Breves, E. (2019). Direct observations of biological carbon export from profiling floats in the subtropical north Atlantic. *Global Biogeochemical Cycles*, 33(3), 282–300. <https://doi.org/10.1029/2018GB006098>
- Fox, J., Behrenfeld, M. J., Haëntjens, N., Chase, A. P., Kramer, S. J., Boss, E., et al. (2020). Phytoplankton Growth and Productivity in the Western North Atlantic: Observations of Regional Variability from the NAAMES field campaigns. *Frontiers Marine Science*, 7, 24. <https://doi.org/10.3389/fmars.2020.00024>
- Garcia, H. E., Locarnini, R. A., Boyer, T. P., Antonov, J. I., Baranova, O. K., Zweng, M. M., et al. (2013). World Ocean Atlas 2013, Volume 4 : Dissolved Inorganic Nutrients (phosphate, nitrate, silicate). *NOAA Atlas NESDIS*, 76, 4. <https://doi.org/10.1182/blood-2011-06-357442.25>
- Graff, J. R., Westberry, T. K., Milligan, A. J., Brown, M. B., Dall'Olmo, G., van Dongen-Vogels, V., et al. (2015). Analytical phytoplankton carbon measurements spanning diverse ecosystems. *Deep Research Part I Oceanography Research Paper*, 102, 16–25. <https://doi.org/10.1016/j.dsr.2015.04.006>
- Hedges, J. I., Baldock, J. A., Gélinas, Y., Lee, C., Peterson, M. L., & Wakeham, S. G. (2002). The biochemical and elemental compositions of marine plankton: A NMR perspective. *Marine Chemistry*, 78(1), 47–63. [https://doi.org/10.1016/S0304-4203\(02\)00009-9](https://doi.org/10.1016/S0304-4203(02)00009-9)
- Laws, E. A., D'Sa, E., & Naik, P. (2011). Simple equations to estimate ratios of new or export production to total production from satellite-derived estimates of sea surface temperature and primary production. *Limnology and Oceanography: Methods*, 9, 593–601. <https://doi.org/10.4319/lom.2011.9.593>
- Laws, E. A., Falkowski, P. G., Smith, W. O., Ducklow, H., & McCarthy, J. J. (2000). Temperature effects on export production in the open ocean. *Global Biogeochemical Cycles*, 14(4). <https://doi.org/10.1029/1999GB001229>
- Liang, J. H., Deutsch, C., McWilliams, J. C., Baschek, B., Sullivan, P. P., & Chiba, D. (2013). Parameterizing bubble-mediated air-sea gas exchange and its effect on ocean ventilation. *Global Biogeochemical Cycles*, 27(3), 894–905. <https://doi.org/10.1002/gbc.20080>
- Maritorena, S., Siegel, D. A., & Peterson, A. R. (2002). Optimization of a semi-analytical ocean color model for global-scale applications. *Applied Optics*, 41(15), 2705–2714.
- Morán, X. A. G., Pérez, V., & Fernández, E. (2007). Mismatch between community respiration and the contribution of heterotrophic bacteria in the NE Atlantic open ocean: What causes high respiration in oligotrophic waters?. *Journal of Marine Research*, 65(4), 545–560. <https://doi.org/10.1357/002224007782689102>
- Morel, A., Huot, Y., Gentili, B., Werdell, P. J., Hooker, S. B., & Franz, B. A. (2007). Examining the consistency of products derived from various ocean color sensors in open ocean (Case 1) waters in the perspective of a multi-sensor approach. *Remote Sensing of Environment*, 111, 69–88. <https://doi.org/10.1016/j.rse.2007.03.012>
- Morel, A., & Maritorena, S. (2001). Bio-optical properties of oceanic waters: A reappraisal. *Journal of Geophysical Research*, 106(C4), 7163–7180. <https://doi.org/10.1029/2000JC000319>
- Westberry, T., Behrenfeld, M. J., Siegel, D. A., & Boss, E. (2008). Carbon-based primary productivity modeling with vertically resolved photoacclimation. *Global Biogeochemical Cycles*(2), 22. <https://doi.org/10.1029/2007GB003078>
- Westberry, T. K., Williams, P. J. le B., & Behrenfeld, M. J. (2012). Global net community production and the putative net heterotrophy of the oligotrophic oceans. *Global Biogeochemical Cycles*, 26(4). <https://doi.org/10.1029/2011GB004094>

- Yang, B., Boss, E. S., Haëntjens, N., Long, M. C., Behrenfeld, M. J., Eveleth, R., & Doney, S. C. (2020). Phytoplankton phenology in the North Atlantic: Insights from profiling float measurements. *Frontiers Marine Science*, 7. <https://doi.org/10.3389/fmars.2020.00139>
- Yang, B., Emerson, S. R., & Angelica Penã, M. (2018). The effect of the 2013-2016 high temperature anomaly in the subarctic Northeast Pacific (the "blob") on net community production. *Biogeosciences*, 15(21), 6747–6759. <https://doi.org/10.5194/bg-15-6747-2018>
- Yang, B., Emerson, S. R., & Quay, P. D. (2019). The Subtropical Ocean's Biological Carbon Pump Determined From O₂ and DIC/DI13C Tracers. *Geophysical Research Letters*, 46(10), 5361–5368. <https://doi.org/10.1029/2018GL081239>